

We are IntechOpen, the world's leading publisher of Open Access books Built by scientists, for scientists

6,900

Open access books available

185,000

International authors and editors

200M

Downloads

Our authors are among the

154

Countries delivered to

TOP 1%

most cited scientists

12.2%

Contributors from top 500 universities



WEB OF SCIENCE™

Selection of our books indexed in the Book Citation Index
in Web of Science™ Core Collection (BKCI)

Interested in publishing with us?
Contact book.department@intechopen.com

Numbers displayed above are based on latest data collected.
For more information visit www.intechopen.com



High-Chromium (9-12Cr) Steels: Creep Enhancement by Conventional Thermomechanical Treatments

Javier Vivas, David San-Martin, Francisca G. Caballero and Carlos Capdevila

Abstract

There is a worldwide need to develop materials for advanced power plants with steam temperatures of 700°C and above which have the capacity to achieve high efficiency and low CO₂ emissions. This request involves the development of new grades of 9-12Cr heat-resistant steels, with a nanostructured martensite, mainly focusing on the long-term creep rupture strength of base metal and welded joints, creep-fatigue properties, and microstructure evolution during exposure at such elevated temperatures. The main shortcomings of actual 9-12Cr high-chromium steels are that the creep resistance is not enough to fulfill the engineering requirements at temperatures higher than 600°C and the material undergoes a cyclic softening. Creep strength at high temperature could be improved by a microstructural optimization through nano-precipitation, guided by computational thermodynamics, and thermomechanical control process optimization.

Keywords: creep-resistant steels, thermomechanical treatment, creep fracture behavior, microstructural degradation, small punch creep tests, ausforming

1. Introduction

There is a worldwide need for the sustainability of current energy sources in order to ensure the viability of future generations, as long as these sources are environmentally friendly. In this sense, power plant designs for the future should ensure a cost-efficient reduction of CO₂ emissions and improvements in efficiency of fuel consumption.

The essential function of a power station is to convert energy from fuel (fossil or nuclear) into electrical energy. In the steam power plant, this conversion involves consuming the fuel to produce heat which is then used to produce steam to drive a turbine. The mechanical energy of the turbine is then converted to electrical energy by an alternator. The steam temperature on the entrance of the turbine is essential to increase the efficiency of the conventional steam cycle.

The maximum steam temperature and pressure are limited by the performance of certain components. The main components which are critical are steam headers,

superheater and reheater tubing in boilers, turbine valve chest, rotors and casings, main steam and reheat pipework, generator rotors, and bolts used for high-temperature applications. The boiler components are limited by corrosion and creep. Pipework also suffers creep as well as weld cracking and thermal fatigue. Turbine components are subjected to creep and fatigue (both thermal and mechanical).

Therefore, the development of improved structural materials to increase in thermal efficiency has been the driving force to develop new generations of 9-12Cr ferritic/martensitic (FM) steels [1–3]. The most relevant in-use properties that heat-resistant steels employed to manufacture components in power plants should fulfill are good mechanical properties, fabricability, corrosion resistance, and creep strength. As indicated above, creep strength has been the most studied and has led to innumerable research activities, aiming at improving the creep strength in 9-12Cr FM steel developments [4–6]. The disadvantage of these steels is their loss of strength beyond 600°C, so they need to be optimized to guarantee their use in the future power plants. In this chapter one of the most promising ideas described is applying a thermomechanical treatment (TMT) instead of a conventional treatment. The main contribution of the TMT is the ausforming, which, as other authors have reported, allows increasing considerably the number density of the thermally stable precipitates, i.e., MX nanoprecipitates. Consequently, the creep strength has improved greatly.

2. Brief remarks on the evolution of 9Cr FM steel for the power-generation industry

As it has been reviewed by Klueh in his seminal work on high-chromium FM steels [7], the design and production of 9-12Cr FM steels began in 1912 when Krupp and Mannesmann produced a 12 wt. % Cr steel containing 2–5 wt. % Mo. This type of steel was used for steam turbine blades, and it is still in use under the designation of X22CrMoV12. The 2¼Cr-1Mo bainitic steel grade normally known as ASTM Grade 22¹ (with nominal composition of Fe-2.25Cr-1.0 Mo-0.3Si-0.45Mn-0.12C) was firstly introduced in fossil fuel power plants in the 1940s and is nowadays widely used. The 9Cr-1Mo FM steel grade (known as Grade 9) is a natural evolution from Grade 22, seeking a better corrosion resistance and, hence, increasing the chromium addition. These two steel grades are the reference steels for heat-resistant application in power plants. Since then, the steady need of pushing up the operating conditions in conventional fossil-fired power-generation systems led to the development of several “generations” of steels with improved elevated-temperature strengths. The evolution of steel compositions (**Figure 1**), which began with G22 and G9 (zeroth generation) with 100,000 h creep rupture strengths at 600°C of about 40 MPa, has allowed for increased operating steam temperatures and pressures [1–3, 8–12]. Three generations of steels have been introduced since the introduction of G22 and G9, and a fourth generation is in development.

The strategy adopted for improved corrosion and oxidation resistance for elevated-temperature operating conditions was the addition of carbide formers such as vanadium and niobium to add precipitate strengthening. Hence, the zeroth generation containing mainly 9-12Cr evolved to the 12Cr-MoV steels introduced in the power plants in the mid-1960s for thin- and thick-walled power station

¹ Grade 22 and the other commercial steels are given designations by ASTM (e.g., Grade 9 is 9Cr-1Mo, and Grade 91 is modified 9Cr-1Mo). The steels are further distinguished as T22 or T91 for tubing, P22 and P91 for piping, F22 and F91 for forgings, etc. The “G” designation will mainly be used here.

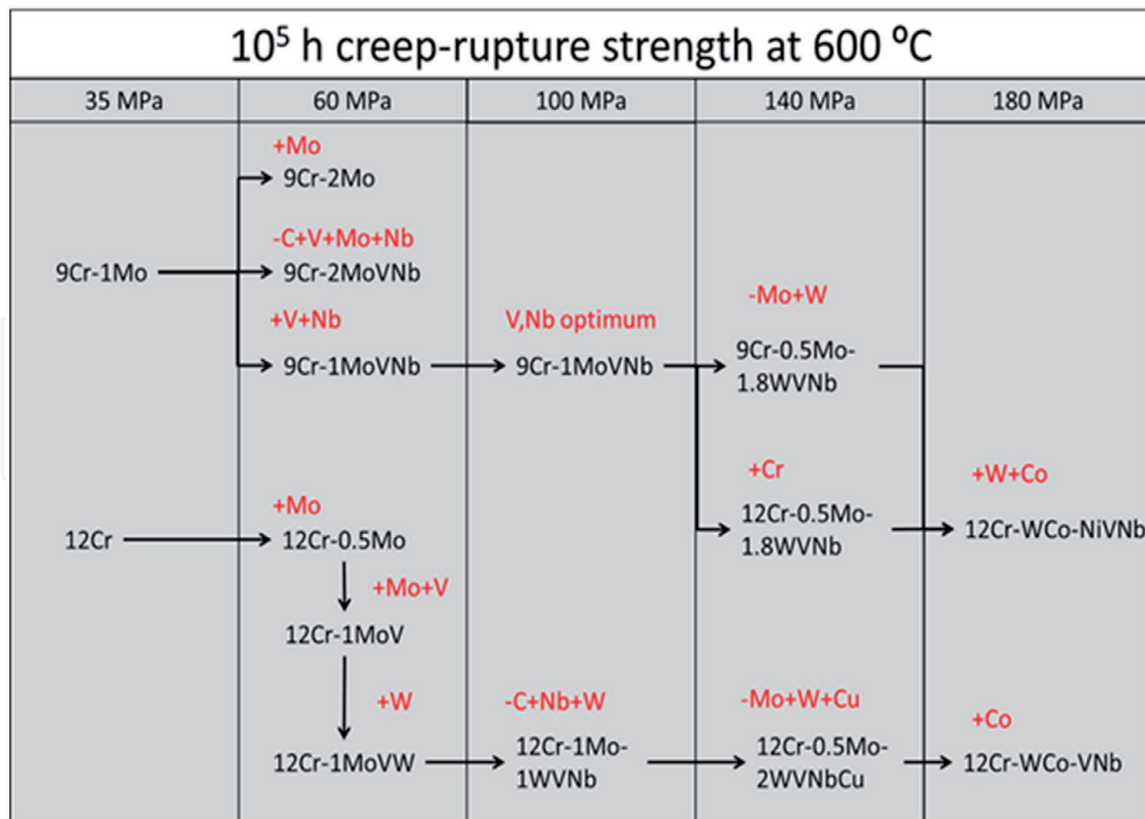


Figure 1.
 Flowchart showing the evolution of 9-12Cr FM steels [7].

components. Their creep strength is based on solution hardening and on the precipitation of $M_{23}C_6$ carbides. These steels have been applied successfully in power stations over several decades [10]. These steels had increased 10⁵ h rupture strengths at 600°C of up to 60 MPa (**Table 1**).

The second generation, developed in the late 1970s, is based on the modified 9Cr-1Mo, designated as G91 and HCM12 (see **Table 1**), which were developed for manufacturing of pipes and vessels for fast breeder reactors [10]. In this steel class, C, Nb, and V contents were optimized, N (0.03–0.05 wt. %) was added, and the maximum operating temperature increased to 593°C. The new steels have a duplex structure (tempered martensite and δ -ferrite). These steels have 10⁵ h rupture strengths at 600°C of about 100 MPa. Of these latter steels, G91 has been used most extensively in the power-generation industry in all new power plants with operational temperatures up to 600°C [7]. The responsible mechanism for this substantial increment of creep strength as compared with 12Cr-MoV steels is the formation of thermally stable V and Nb carbonitrides. Besides lowering the Cr content down to 9 wt. %, tempered martensite microstructure also contributes to the higher creep strength [13, 14].

The Japanese steel development program led by Nippon Steel achieved the development of the P92 steel (NF616). This steel grade, designated as Grade 92, presents a further increases in stress rupture by the addition of 0.003 wt. % B and 1.8 wt. % W and reducing the Mo content from 1 to 0.5 wt. % [15, 16]. The addition of B ensures thermally stable $M_{23}(C,B)_6$ precipitates, whereas the higher W content leads to a higher amount of precipitated Laves phase [17, 18]. Grade 92, firstly introduced in the 1990s along with equivalent steel such as E911, fulfills the niche of steam operational temperature of 620°C for 10⁴ h creep rupture strengths at 140 MPa.

Finally, the goal for the next steel generation being developed at present is pushing the limit of operation temperature above 650°C. This so-called fourth generation differs from the previous ones mainly by the addition of 3.0 wt. % Co

Country	Steel	Chemical composition (wt.%)									Rupture strength at 600°C (MPa)	
		C	Cr	Mo	Ni	W	V	Nb	N	B	10 ⁴ h	10 ⁵ h
	Basics											
Germany	X22CrMoV12-1	0.22	12.0	1.0	0.5	-	0.3	-	-	-	103	59
UK	9Cr-1Mo (Grade 9)	0.10	9.5	1.0	0.2	-	-	-	-	-	-	-
UK	H46	0.16	11.5	0.65	0.7	-	0.3	0.3	0.05	-	118	62
France	54T5	0.19	11.0	0.8	0.4	-	0.2	0.45	0.05	-	144	64
Japan	TAF	0.18	10.5	1.5	0.1	-	0.2	0.15	0.01	0.035	216	(150)
USA	11%CrMoVNbN	0.18	10.5	1.0	0.7	-	0.2	0.08	0.06	-	165	(85)
	Advanced											
USA	G91	0.1	9.0	1.0	<0.4	-	0.22	0.08	0.05	-	124	94
Japan	HCM12	0.1	12.0	1.0	-	1.0	0.25	0.05	0.03	-	-	75
Japan	TMK2	0.14	10.5	0.5	0.5	1.8	0.17	0.05	0.04	-	185	90
Europe	X18CrMoVNB 91	0.18	9.5	1.5	0.05	-	0.25	0.05	0.01	0.01	170	122
Europe	X12CrMoWVNbN	0.12	10.3	1.0	0.8	0.8	0.18	0.05	0.06	-	165	90
EU Cost501	E911	0.11	9.0	0.95	0.2	1.0	0.20	0.08	0.06	-	139	98
Japan	P92	0.07	9.0	0.50	0.06	1.8	0.20	0.05	0.06	0.003	153	113
Japan	P122	0.1	11.0	0.4	<0.40	2.0	0.22	0.06	0.06	0.003	156	101
Japan	HCM2S	0.06	2.25	0.2	0.2	-	0.25	0.05	0.02	0.003	-	80
Germany	7CrMoTiB	0.07	2.40	1.0	1.0	-	0.25	-	0.01	0.004	-	60
EU Cost522	FB2	0.13	9.0	1.5	0.15	-	0.20	0.05	0.02	0.0085	-	125
EU Cost522	CB2	0.12	9.0	1.5	0.15	-	0.20	0.06	0.02	0.011	-	125

Table 1.

Chemical composition and creep rupture strength at 600°C of the 9-12Cr heat-resistant steels from 1950 to 2005 [19].

as an austenite stabilizer because of the adverse effect of nickel on creep. They have projected 10⁵ h creep rupture strengths at 600°C of 180 MPa [7]. In these steels with about 0.1 wt. % carbon, molybdenum has been further reduced or eliminated, and tungsten (2.6–3.0 wt. %) has been increased compared to third-generation compositions. In **Table 1**, an overview of the historical development of the 9-12Cr heat-resistant steels from 1950 to 2005 is shown.

2.1 Creep deformation

Creep deformation is a thermally activated process, and the rate of deformation (creep rate) is extremely temperature sensitive. In metals, creep deformation becomes important at temperatures greater than about 0.4T_M, where T_M is the absolute melting temperature [20]. In the case of 9-12Cr FM steels, this temperature is approximately 450°C. Clearly, power plant materials operate in the temperature regime where creep process is significant. The creep properties of the material used limit the operating temperature of many power plant components, such as the turbines. Development of materials with an increased creep resistance is central to the use of power plants with higher steam temperatures.

Creep deformation can occur by a variety of different mechanisms. The mechanism that dominates depends on the stress and temperature conditions as well as the microstructure of the material.

In the case of power plant steels, the stress levels are relatively high, and the temperatures (compared with melting point) are relatively low. In the case of creep deformation, it is controlled primarily by dislocation movement and the thermal energy available for dislocations to overcome obstacles. A deformation mechanism map gives information about which mechanism will dominate for a particular set

of conditions. Such a diagram for a G91 steel is shown in **Figure 2**. For the exposure conditions, for this material, a power law creep (dislocation creep) is expected to dominate.

Power law creep involves the movement of dislocations, and the creep rate is a result of the balance between work hardening and recovery. Work hardening results in an increase in the dislocation density, while recovery leads to a reduction in the dislocation density. If the dislocation density remains constant, then the creep rate is given by Norton's law [21]:

$$\dot{\epsilon} = A (\sigma_a + \sigma_l + \sigma_u + \sigma_g)^4 \quad (1)$$

In this equation σ_a is the applied stress, σ_l , σ_u , and σ_g are the internal stresses due to solution, precipitation, and grain boundary hardening, respectively. The most effective method for reducing the creep rate is therefore to form a suitable distribution of particles which are also able to act as barriers to dislocation motion.

A study of the possible creep mechanisms suggests microstructures would be expected to have good creep resistance under conditions used in power plant. In general, creep-resistant alloys are based on a matrix which is a solid solution. The presence of misfitting solute atoms in solid solution makes the passage of dislocations through the matrix more difficult. However, the majority of the creep resistance, at least in the early stages of service, is derived from precipitate particles. Ideally these particles should be small, and they should be widely and homogeneously distributed in large numbers through the matrix. The particles need to be stable at operating temperatures for which the alloy is designated, and they should be resistant to coarsening, as this will reduce their effectiveness as strengtheners. In general, excessive work hardening and very fine grain sizes, which provide strengthening at ambient temperatures, are considered detrimental in high-temperature alloys. This is because both of them provide easy diffusion paths and therefore lead to an increase in the creep rate.

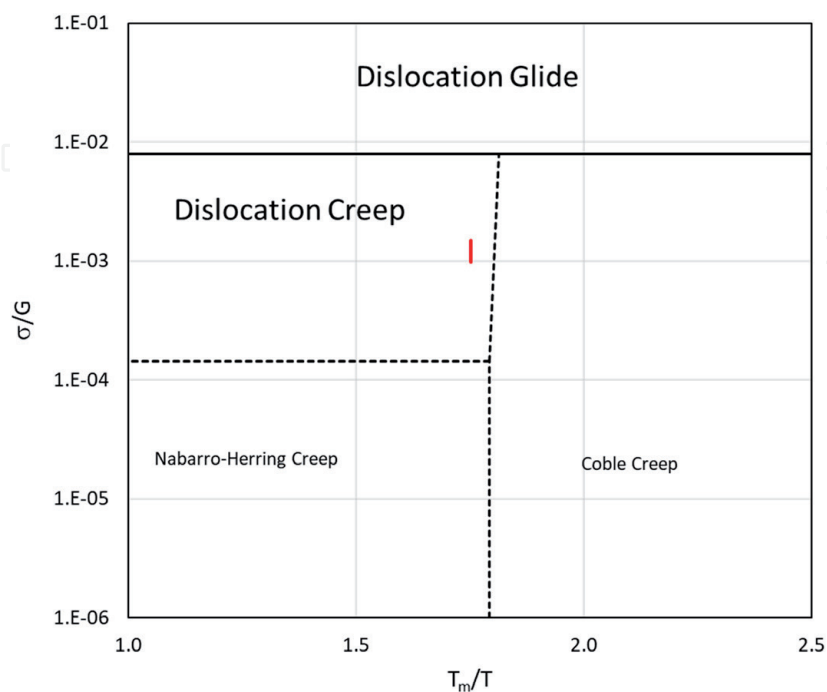


Figure 2. Deformation mechanism map (D-MAP) of T91 steel calculated from experimental reported values [22, 23]. The red line indicates the experimental conditions considered in this work.

2.2 Creep and microstructural evolution

The new environmental regulations and commercial needs of the industry are the driving force for the development of new heat-resistant steels that push forward the operational limits of current steels. In this framework, the high-Cr FM steels applied as structural materials in fossil-fired and in nuclear power plants need to implement the operating temperatures above 650°C [1–3, 8–12]. The mechanism responsible for creep strengthening in these steels is the solid-solution and dispersion strengthening.

In the particular case of the so-called 9Cr FM steels, the creep degradation is a consequence of the thermal evolution of their hierarchical martensitic microstructure constituted by prior austenite grains, martensitic packets, blocks, and laths [24]. The microstructural degradation during creep consists of the coarsening of the lath structure [12, 24]. Such coarsening is governed by the subgrain boundary formation and evolution inside the laths, which can be prevented at high temperatures, and virtually frozen, by the dispersion of proper precipitates. The precipitates pin boundary migration and dislocation motion, slowing down the degradation of the martensitic microstructure and hence reducing creep rates [25, 26].

There are two main actors for the microstructural stability driven by precipitation in 9Cr FM steels: The first one is the coarse $M_{23}C_6$ carbides located mainly at the grain boundaries either from the prior austenitic grains or from the blocks or martensite lath boundaries. The second one is the V- and Nb-rich MX carbonitrides. Contrary to $M_{23}C_6$, those MX precipitates are homogeneously distributed within martensite laths. Therefore, the ideal situation would consist of reducing the presence of the $M_{23}C_6$ carbides to the minimum since their fast coarsening induces crack formation at the particle-matrix interface and promoting the formation of MX carbonitrides (nanometric in size), since they will delay the lath coarsening as mentioned above; it has been studied extensively [27–29].

Thermomechanical processing of 9Cr FM steels has been revealed as a promising tool to promote a high number density of MX carbonitrides [30–38]. TMT involves different steps that need to be optimized to produce the most favorable precipitate microstructure for elevated-temperature strength.

2.3 Creep tests

The creep behavior of a material may be characterized by a number of different parameters which can be measured by performing the appropriate creep test. For metallic materials most creep tests are conducted in uniaxial tension with a dumb-bell-shaped specimen similar to that used for tensile testing. The tests are carried out at a constant temperature and under either a constant load or stress. Applying a constant stress is more useful if the test is being employed to provide information about a creep mechanism.

The conventional treatments (AR) and TMT considered in this work were carried out on 10 mm in length and 5 mm in diameter cylindrical samples using a DIL 805A/D plastodilatometer (TA instruments) as described elsewhere [39, 40]. Due to the limited amount of material available after the TMT is carried out in the plastodilatometer, the creep properties were investigated by means of the small punch creep test (SPCT) performed at 700°C as it has been previously reported [41, 42]. The SPCT samples were cut transversally, from cylindrical specimens, with a thickness of 600 μm and a diameter of 8 mm. Then, the disks were ground on both sides down to a final thickness of 500 μm . In the setup of the SPCT, the lower and upper dice are connected via a thread to ensure the clamping of the sample. The load is applied by a ceramic punch ball which is in contact with the sample. A plunger rod is used to transmit the dead weight load to

the punch ball. All these components are made of Al_2O_3 ceramics. The clamping device is surrounded by an electrical heater and a thermal insulation. The upper plate carrying the additional dead weight is guided by two pillars with ball bearings. The temperature is measured in the lower die directly under the sample. The displacement is measured by a capacitive sensor between the upper plate and the thermal insulation with an accuracy of $\pm 1 \mu\text{m}$. A load cell is placed between the upper plate and the plunger rod.

The disk deflection vs. time resulting from the SPCTs might be divided into three different regions similarly to conventional strain vs. time creep curves obtained from uniaxial testing. However, the failure in SPCTs occurs away from the load line with cracks propagating in a circumferential direction due to membrane stretching. Therefore, the first part of the disk deflection vs. time curve corresponds to the loading region where the spherical indenter loads on a very small contact area of the sample. Since the stresses will be higher than the yield stress of the material, local plasticity and an initial large deformation are produced. This large deformation is accumulated in a short period of time. The second stage corresponds to the steady-state region, which coincides with most of the sample life, where the disk deflection rate reached almost a minimum. Finally, the third stage consists of an acceleration of disk deflection and fracture region. The interpretation of this behavior is that once a crack propagates to a critical length, the sample is no longer in balance, leading to an increase in deflection rate and to a reduction in the structure stiffness in the tertiary region. Another explanation might be due to the localized necking without crack presence. The deformation mechanism in the tertiary region is a mixture among accumulation of creep damage, geometric softening, and crack growth effect.

3. Effect of thermomechanical control processing on microstructure

As it has been introduced in previous sections, the pioneer commercial 9-12Cr steels present an upper service temperature of 540°C , which was successfully increased in the late 1970s up to 595°C with the introduction of vanadium and niobium microalloying in the composition of the steel. This steel was used as a benchmark for the development of steels with upper-use temperatures of $600\text{--}620^\circ\text{C}$.

However, it is difficult keep pushing the higher operating temperature too much. Therefore, to continue to exploit the advantages of ferritic steels, oxide dispersion-strengthened (ODS) steels [43–46] were introduced. The first successful alloy was presented in the 1960s, and, since then, it has been an active research field. ODS steels are strengthened by small oxide particles, but the complicated and expensive manufacturing route avoided the full implantation as structural material in the current power plants.

Despite being around for about 40 years, the ODS steels are still in the development stage because of having mechanical property anisotropy [43, 45, 47–49]. Therefore, an alternative strategy to achieve a high number density of precipitates is needed. In this section, we present preliminary results that allow us to conclude that conventional thermomechanical control processing strategy is adequate to achieve dispersion-strengthened steels.

3.1 Microstructure after conventional heat treatment

Lath martensite is a particular microstructure that ensures microstructural stability. Furuhashi and Miyamoto [50] described the variety of crystalline size in lath martensite structures. A hierarchy of lath martensite structure is clearly identified particularly in low-carbon steels. A prior austenite (γ) grain is divided into “packets,” each of which consists of a group of martensite laths with the same

parallel close-packed plane relationship in the Kurdjumov-Sachs (K-S) orientation relationship, denoted as “CP group” recently. In general, a packet is partitioned into several blocks, each of which contains laths of a single variant of the K-S relationship. Blocks and packets are mostly surrounded by high-angle boundaries, whereas lath boundaries inside a block are of low-angle type.

The microstructure resulting from conventional industrial heat treatment consists of tempered martensite, which presents elongated subgrains with an average size of 0.25–0.5 μm (**Figure 3**). Two types of precipitates, M_{23}C_6 carbides rich in chromium and MX carbonitrides rich in V or Nb, are present in the microstructure. The size of M_{23}C_6 carbides is around 100–200 nm, and they are precipitated on subgrain boundaries and prior austenitic grain boundaries. The size of MX carbonitrides is much smaller than M_{23}C_6 carbides, 20–50 nm, and they are in the matrix [51]. The purpose of this work is to produce a dispersion of nanosized precipitates by a controlled TMT, bearing in mind that a high number density of fine MX precipitates (Nb-MX and V-MX) should display superior high-temperature performance.

3.2 Effect of austenitization temperature

The effect of austenitization temperature on the temper microstructure of G91 steel is analyzed in this section. **Figure 4** schematically illustrates the two alternative processing routes considered:

- High austenitization temperature (HAT): In order to achieve an almost complete solid solution in austenite of most of the potential MX precipitate formers, the austenitization condition set will imply an elevated temperature.
- Thermomechanical treatment: The combined effect of the elevated austenitization temperature and a subsequent deformation will be studied with the aim of optimizing the MX-nanoprecipitate distribution during tempering of the martensitic microstructure.

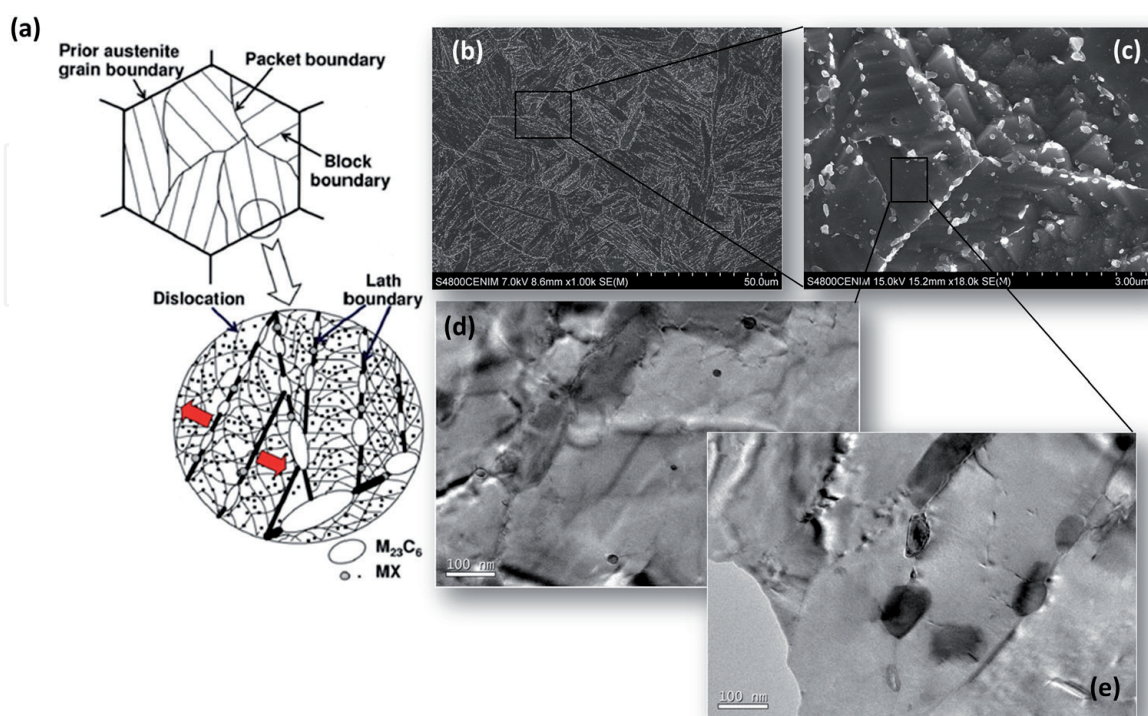


Figure 3. (a) Resulting hierarchy microstructure achieved by conventional heat treatment; (b) and (c) SEM micrographs of the as-received state; (d) and (e) TEM micrographs. Arrow heads point out the location of the M_{23}C_6 carbides on lath boundaries and MX carbonitrides within the laths [37].

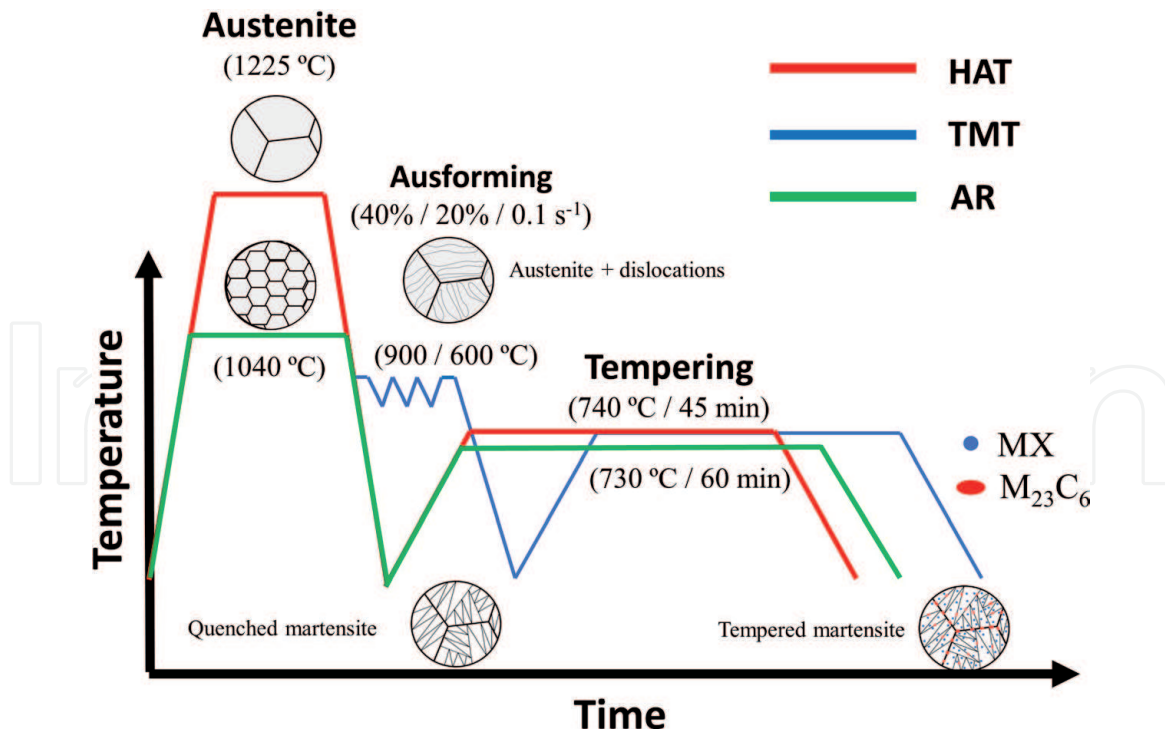


Figure 4.
Thermomechanical treatments investigated in this study [40].

For the sake of comparison, **Figure 4** also includes the industrial manufacturing conditions for G91 steel named as-received (AR) condition. The goal of exploring the effect of austenitization temperature on the microstructure is to enhance the precipitation of nanoparticles during the subsequent tempering stage indicated in **Figure 4**. As it was mentioned above, the main cause for creep softening in conventional G91 is due to the recovery of the martensitic lath microstructure because of mechanisms, such as the dislocation movement, controlled by diffusion [12, 27]. The dislocation pinning by nanosized MX precipitates can delay this phenomenon, since they present an enhanced ripening resistance [8, 52–54]. The goal of undergoing such elevated temperatures in the HAT treatment as compared to conventional austenitization heat treatment (AR treatment) is to dissolve all the primary carbides in the microstructure and drive to solid solution all the potential carbide former elements. Therefore, the martensite formed after quenching from such elevated austenitization temperature keeps in solid solution most of the precursor elements of MX carbides (M = Nb, V; X = C, N) that might precipitate during the subsequent tempering.

It is important to consider that the austenitization temperature has to be high enough to eliminate as much as possible the primary carbides formed during the casting process, but lower than the delta ferrite formation temperature, in order to avoid the detrimental effect of this phase from a long-term creep property point of view. Computational thermodynamic calculations by means of Thermocalc® determine the optimum austenitization temperature in 1225°C (**Figure 5**).

The interest of TMT relies on the role that austenite deformation has on refining the martensitic microstructure [55, 56]. Depending on the deformation temperature, several are the mechanisms that affect the austenite microstructure, and hence, that could be transferred to the martensite upon quenching. If deformation temperature is above the non-recrystallization temperature, the freshly formed austenite microstructure will present a significantly reduced grain size that would induce the concomitant martensitic microstructural refinement. Similarly, by applying plastic deformation to the austenite at temperatures below the non-recrystallization temperature, which is the so-called ausforming processing [57],

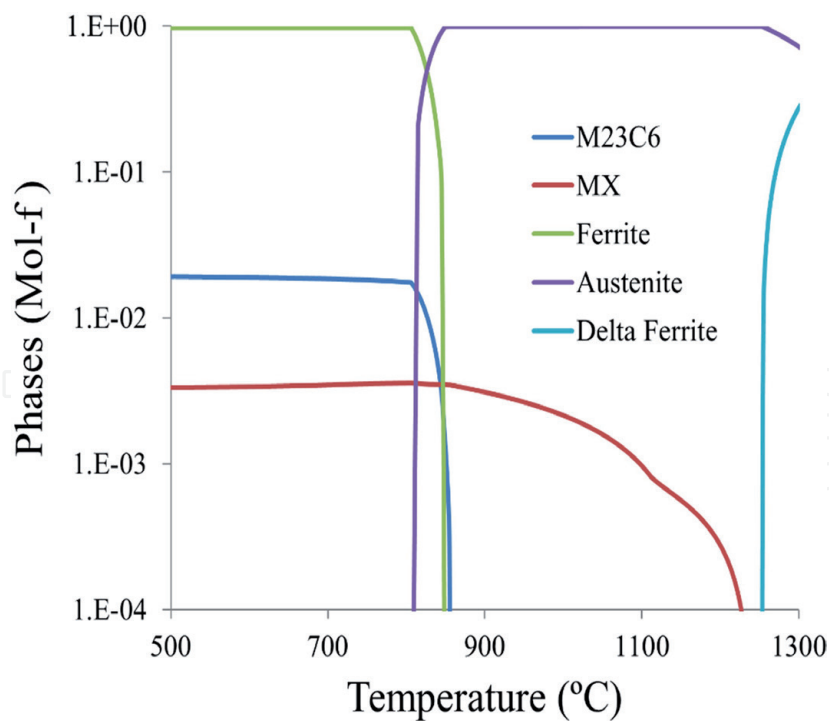


Figure 5.
Temperature evolution of phase mole fraction in G91 calculated by Thermocalc® [38].

an austenitic microstructure with a high population of deformation bands will be formed. This would directly induce the preferential formation of some specific martensitic variants upon austenite transformation (martensite variant selection), leading to the development of strong transformation texture.

Figure 6 illustrates the IPF maps, SEM and TEM micrographs after HAT and TMT processing routes, and the reference (AR) condition. The first conclusion obtained is the coarsening of the block size (white arrows in **Figure 6**) in HAT and TMT conditions as compared with AR condition, because of the high austenitization temperature. Block widths of $2.7 \pm 0.2 \mu\text{m}$ for AR condition were obtained; meanwhile, values of $4.12 \pm 0.37 \mu\text{m}$ for HAT and $3.21 \pm 0.27 \mu\text{m}$ for TMT were measured. The coarser the prior austenite grain, the coarser the block size. However, it is worth noting that finer block size is observed after TMT than with HAT, which is consistent with the fact that thermomechanical processing increases the low-angle substructure and decreases the block size of as-quenched martensite.

The dislocation density after HAT and TMT was measured by XRD [40]. The results show a dislocation density of $(14 \pm 0.1) \times 10^{14} \text{ m}^{-2}$ and $(28 \pm 0.1) \times 10^{14} \text{ m}^{-2}$ after austenitization and ausforming, respectively. One might conclude from these results that the dislocation density in the as-quenched martensite after the TMT is substantially increased as compared with conventional treatment. A similar effect of the ausforming on the dislocation density was reported by other authors [58, 59]. Finally, TEM examination of the microstructure allowed us to determine the lath width of the martensitic microstructure. Values of $360 \pm 35 \text{ nm}$ for AR condition, $350 \pm 20 \text{ nm}$ for HAT condition, and $318 \pm 32 \text{ nm}$ for TMT condition were obtained, which are significantly finer than those reported after conventional treatments, i.e., lath size ranging from 300 to 500 nm [60].

The distribution of M_{23}C_6 precipitates in the tempered martensitic microstructure is also worth analyzing. **Figure 6** illustrates the distribution of M_{23}C_6 carbides after AR, HAT, and TMT processing routes. Coarse and closely spaced M_{23}C_6 carbides, about 70 to 500 nm, were observed. The number density and average particle size of these carbides were determined by studying several SEM micrographs to determine values of $6.19 \times 10^{19} \text{ m}^{-3}$ and $141 \pm 3 \text{ nm}$ for AR condition, $8.24 \times 10^{19} \text{ m}^{-3}$

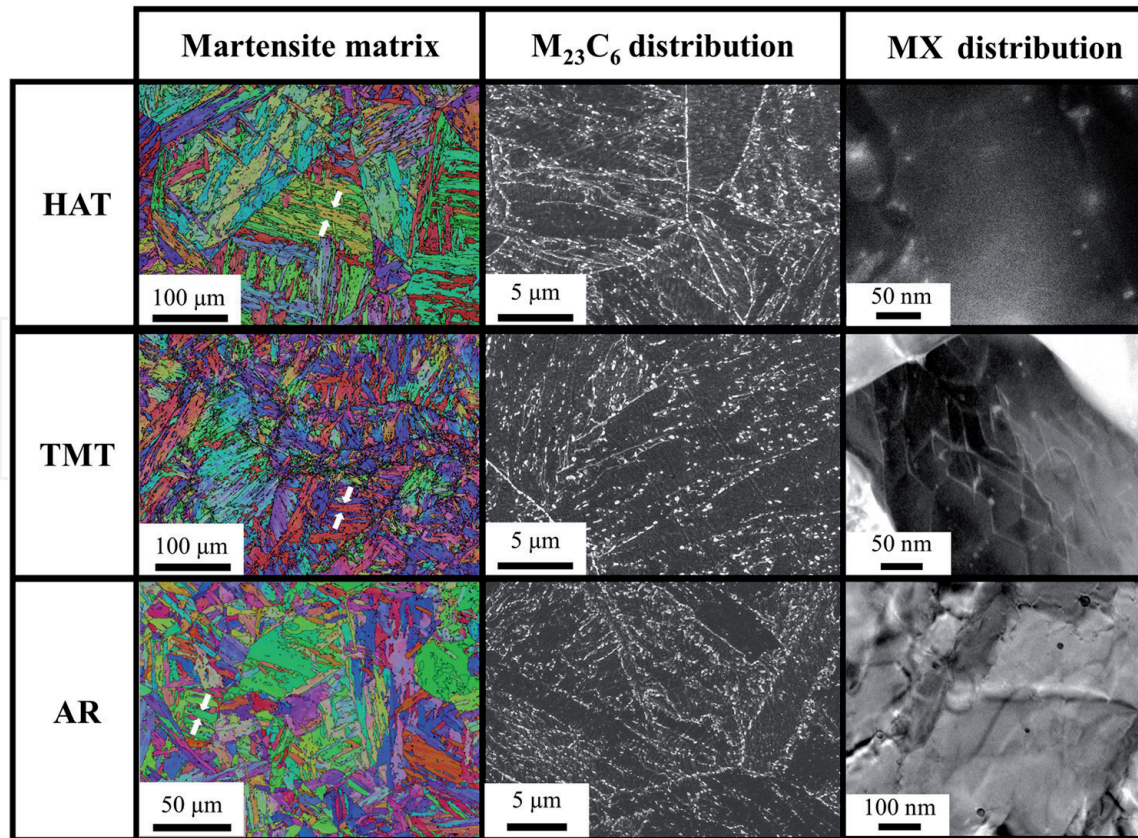


Figure 6.
 Martensite matrix, M₂₃C₆ precipitate, and MX-nanoprecipitate distributions after the different thermomechanical and heat [40].

and 124 ± 3 nm for HAT condition, and $4.11 \times 10^{19} \text{ m}^{-3}$ and 143 ± 5 nm for TMT steel. These values are very similar to those reported by Klueh et al. for the steel after conventional heat treatment [35].

On the contrary, the finely dispersed MX nanoprecipitates present inside the martensitic laths and associated with dislocations are also observed in **Figure 6**. Therefore, this result suggests the role of dislocations as potential nucleation sites for MX nanoprecipitates. Hence, the importance of ausforming in generating a homogeneous distribution of nanosized MX particles in the microstructure might be also foreseen. These spherical MX nanoprecipitates had a mean particle size of 12 ± 1 nm with a number density of $7.20 \times 10^{21} \text{ m}^{-3}$ for HAT steel and 9 ± 1 nm with a number density of $1.86 \times 10^{22} \text{ m}^{-3}$ for TMT steel. The MX precipitates are, in both cases, significantly smaller than those measured after AR condition, i.e., particle size of 25 ± 5 nm with a number density of $8.14 \times 10^{19} \text{ m}^{-3}$. The size values obtained after HAT and TMT are smaller, and the number density higher, than measurements reported in the literature after conventional heat treatments [61].

Figure 7 shows the disk deflection versus time curves obtained for the three conditions studied (AR, HAT, and TMT) at 700°C with a load of 200 N. The curves exhibit the three stages of creep that were described in previous sections. The first stage corresponds to the loading region where the spherical indenter loads the sample, and the mode of deformation is by bending. The second stage is characterized by a decrease in deflection rate and corresponds to the steady-state region with a minimum disk deflection rate. Finally, the third stage consists of an acceleration of disk deflection and fracture region. In the secondary and tertiary stages, stretching is the prominent deformation mode. Once a crack propagates to a critical length, the sample is no longer in balance, leading to an increase in deflection rate and to a reduction in the structure stiffness in the tertiary region until the final fracture.

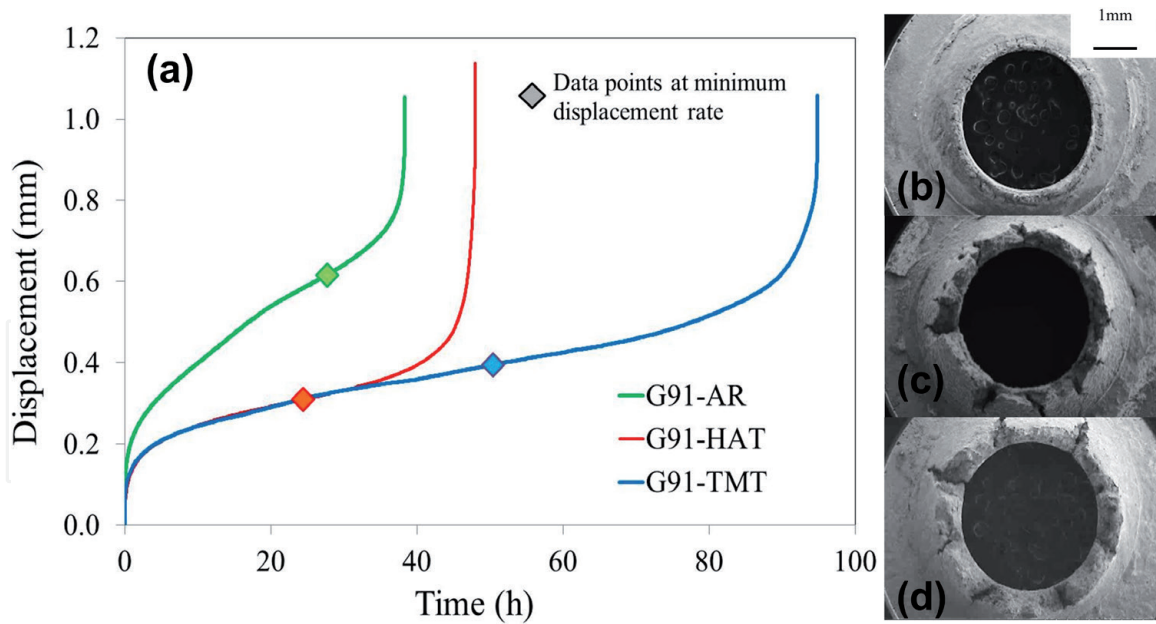


Figure 7.

(a) SPCT curves measured for the samples after the different thermomechanical and heat treatments and the creep fracture micrographs for the (a) AR, (b) HAT, and (c) TMT [40].

As indicated above, the minimum disk deflection rate (δ_d) is an important parameter that can be evaluated by SPCT. The evolution of disk deflection rate with the applied load might be described by an equivalent expression to the conventional Norton's power law for creep, which is similar to the expression used in Eq. (1):

$$\delta_d = A \cdot F^n \quad (2)$$

where A is a temperature-dependent constant, F is the force applied on the specimen, and n is the force exponent. One might conclude, therefore, from **Figure 7** that the creep strength has significantly improved after the TMT condition. The time to rupture was 2.5 and 1.24 times greater than AR condition, from 38 to 95 h and 48 h for the TMT and HAT, respectively. The δ_d was $2.9 \mu\text{m}\cdot\text{h}^{-1}$ for the TMT sample, while for the HAT sample, it was $3.7 \mu\text{m}\cdot\text{h}^{-1}$. These minimum disk deflection rates were significantly slower than the minimum disk deflection rate measured for the G91 in the AR condition, which was $9.5 \mu\text{m}\cdot\text{h}^{-1}$.

The results obtained suggest that the increase in the number density of MX precipitates enhances the strengthening capability at high temperature, since they are able to pin more effectively the dislocations. Hence minimum creep rate is reduced and the onset of tertiary creep is retarded. The differences in minimum disk deflection rate and time to rupture between the sample after TMT and HAT support the importance of ausforming on improving creep resistance.

3.3 Effect of ausforming

The next stage in the TMT after austenitization is the ausforming as shown in **Figure 4**. The effect of ausforming on low-carbon lath martensitic microstructure has been already described by Miyamoto et al. [62]. The authors reported that martensite variants with habit planes that are nearly parallel to the close-packed primary and secondary slip planes in austenite transform preferentially, i.e., martensite habit planes such as $(575)\gamma$ that are nearly parallel to $(111)\gamma$ and $(-111)\gamma$ in austenite [63]. Since strain is accumulated preferentially in $(111)\gamma$ and $(-111)\gamma$ slip planes during ausforming, this results in an increasing number of dislocation

that might be transferred to martensite (011)_M planes. Therefore, ausforming might increase the dislocation density in the resulting martensitic microstructure.

On the other hand, Takahashi et al. [64] reported recently the formation of Nb-cottrell atmospheres in low-carbon Nb-microalloyed steels. The authors explained that this mechanism is based on the fact that segregation energy of Nb to edge dislocation core was almost the same as the energy for grain boundary segregation. Besides, the large attractive interaction between Nb and dislocation core was due to its large atomic size. Therefore, such interaction between Nb atoms and dislocations retards the recovery of dislocation at high temperatures and, hence, stabilizes the microstructure at high temperatures. It might be expected that Nb presents the same behavior in the studied steel, preventing recovery after ausforming and promoting the fine and homogeneous MX carbonitride precipitation during tempering accordingly.

In this work the role of ausforming temperature by selecting 600 and 900°C, at a constant deformation of 20% (**Figure 4**), is explored. As mentioned above, the dislocation densities were estimated by XRD in fresh martensite after each ausforming condition studied [41]. Values of $(2.8 \pm 0.1) \times 10^{15} \text{ m}^{-2}$ and $(1.9 \pm 0.1) \times 10^{15} \text{ m}^{-2}$ were obtained for the ausforming at 600 and 900°C, respectively. These results show that the lower the ausforming temperature, the higher the dislocation density introduced in austenite is, which might be due to the fact that some of the dislocations in fresh martensite are inherited from deformed austenite as it was mentioned above.

On the other hand, Bhadeshia and Takahashi reported [65] an expression that allows to estimate the dislocation density (ρ_d):

$$\text{Log } \rho_d = 9.28480 + \frac{6880}{T} - \frac{1780360}{T^2} \quad (3)$$

This expression is valid only when the martensite start temperature (T) is between the range 297 and 647°C.

Extracting the data of the martensite start temperature from a previous work [38], the estimation of the dislocation density obtained after the different ausforming conditions can be estimated. In this sense, ausformed samples at 600°C present a martensite start temperature of 338°C; introducing this value in Eq. (3), a dislocation density of $5.97 \times 10^{15} \text{ m}^{-2}$ is calculated. Similarly, for the material ausformed at 900°C with a martensite start temperature of 374°C, the dislocation density calculated is $4.62 \times 10^{15} \text{ m}^{-2}$. These results are in the same order of magnitude than those measured by X-ray diffraction, which demonstrate that the ausforming increases the dislocation density in the martensite.

During the final stage (tempering), MX carbonitrides and M₂₃C₆ carbides precipitate, and the recovery of dislocations takes place. Because of the higher dislocation density of ausformed samples, the number density of finer MX increases, and these precipitates are found homogeneously distributed within laths, as it can be seen in **Figure 8(a)** pointed out by white arrows.

The number density of MX precipitates (N) was determined through the direct measurements of spacing (λ) between MX carbonitrides from several TEM micrographs as indicated by Eq. (4):

$$N = 1/\lambda^3 \quad (4)$$

Figure 8(b) shows the size distribution of the precipitates in ausformed material. In the material ausformed at 600 and 900°C, the average size of MX carbonitrides was 5.6 nm and 7.4 nm, respectively. The number density of MX carbonitrides was $9.39 \times 10^{22} \text{ m}^{-3}$ for the material ausformed at 600°C and $6.4 \times 10^{22} \text{ m}^{-3}$ for the material ausformed at 900°C. On the other hand, the reported values of the size and number density of MX carbonitrides after the conventional processing were 30 nm

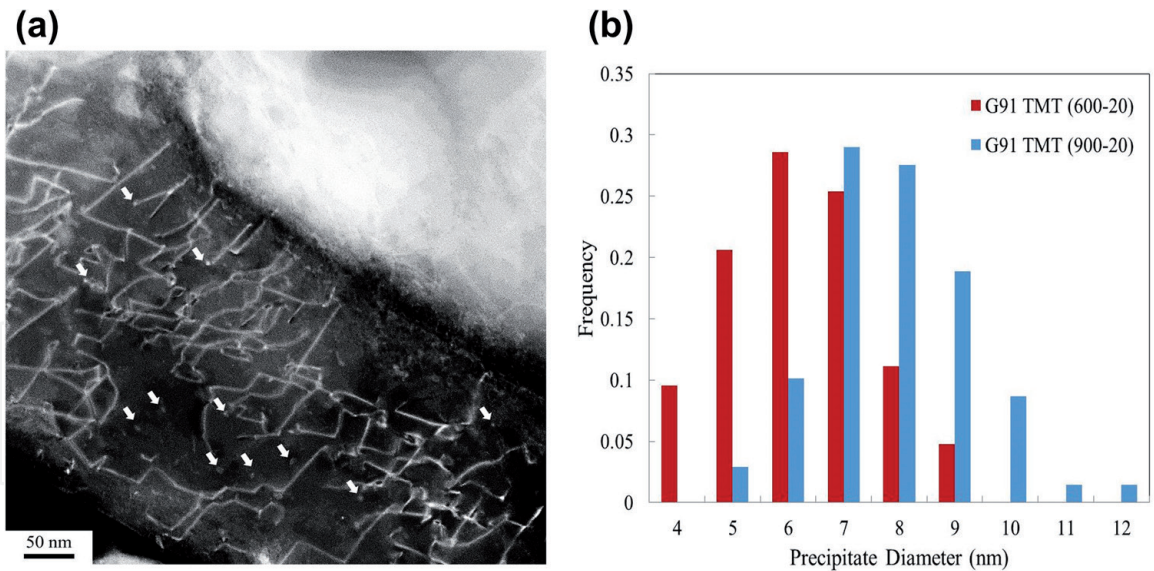


Figure 8. (a) MX carbonitrides (white arrows) within laths after thermomechanical treatment ausformed (20%) at 900°C; (b) size distribution of MX precipitates in the TMT samples for the two ausforming temperatures: 600 and 900°C [41].

and 10^{20} m^{-3} , respectively [61]. It might be concluded that ausforming promotes a refining of precipitates, up to five times as compared with conventional processing, as well as an increase in number density up to two orders of magnitude. In fact, these number densities and precipitate sizes are very similar compared to those corresponding to oxides present in oxide dispersion-strengthened (ODS) steels [66, 67].

The elevated number density of nanosized MX precipitates has a direct impact on creep response of this material as it can be clearly observed in **Figure 9**. This figure shows characteristic SPCT curves at 200 N, exhibiting the variation of specimen deflection with time. It might be concluded from this figure that introducing an ausforming step improves the δ_d significantly, and most precisely, the lower the ausforming temperature, the lower the δ_d is, and, hence, the better the creep resistance is.

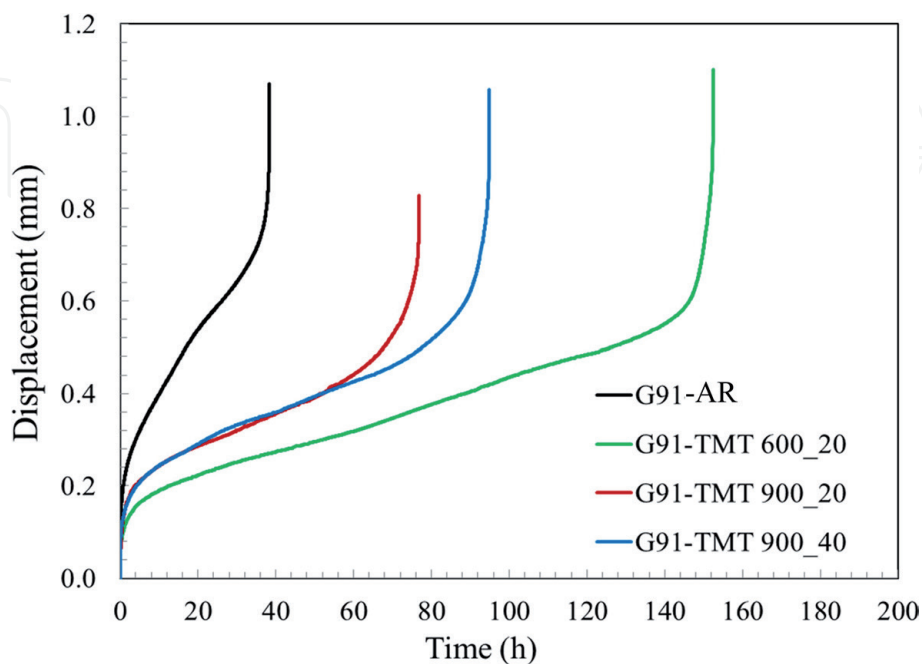


Figure 9. SPCT curves for all samples tested at 700°C with a load of 200 N [39].

4. Failure mechanism: post-creep characterization of SPCT samples

Scanning electron microscopy (SEM) images of fractured SPCT specimens for different conditions are shown in **Figure 10**. Radial cracks can be observed in all the TMT samples (**Figure 10a–c**). This is an evidence of the loss of ductility and indicates a brittle fracture, which is a change in rupture ductility in comparison to the conventionally treated sample. Those samples do not show radial cracks (**Figure 10d**). Besides, a higher reduction in thickness is evident in the conventionally treated sample in comparison to the TMT ones, suggesting a ductile fracture behavior.

To clarify the failure mechanisms, the fractured samples were cut and prepared adequately. **Figure 11(a)** and **(b)** shows the SEM images for the TMT samples ausformed at 600°C with a deformation of 20% and ausformed at 900°C with a deformation of 40%. It is worth noting in those images the existence of cavities nearby coarse particles, which are located at the vicinity of PAGBs. The EDS spectrum shown in **Figure 11(c)** allows us to conclude that these particles are $M_{23}C_6$ carbides with $M = (Fe, Cr, Mo)$.

The greater size of the $M_{23}C_6$ carbides at the vicinity of PAGB contributes to the inhomogeneous and localized deformation experienced by the TMT samples at these locations during creep. The local creep concentration close to PAGB would be promoting the nucleation of cavities that lead to the intergranular fracture with the brittle behavior.

Figure 12 shows different inverse pole figure (IPF) maps for all the samples under study before and after SPCT. It should be pointed out that, contrary to the lath boundaries that are not correctly indexed due to the step size used for the EBSD mapping, the block boundaries before and after SPCT are clearly disclosed. It is observed that the microstructures of the samples exhibit the characteristic lath-like morphology of the martensitic microstructure. However, such morphology is

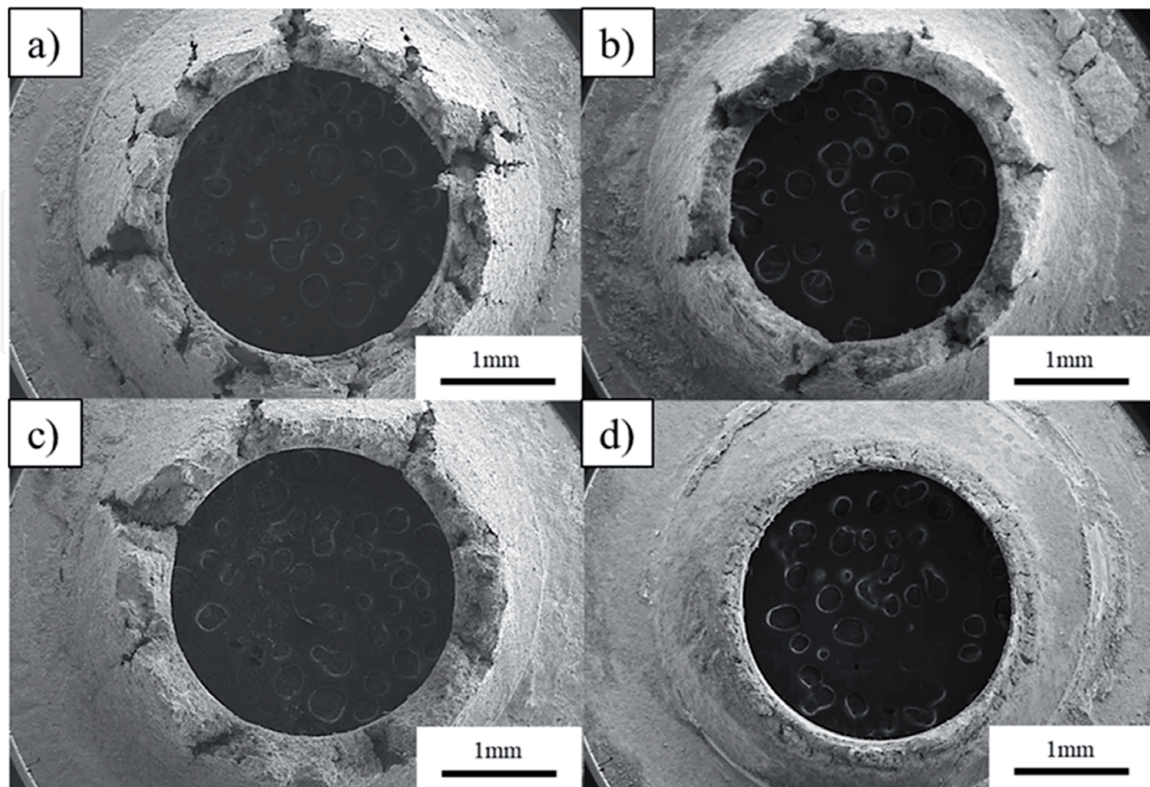


Figure 10. Scanning electron microscopy images of the SPCT fracture surfaces for samples tested at 700°C with a load of 200 N: (a) G91-TMT 900_20; (b) G91-TMT 600_20; (c) G91-TMT 900_40; and (d) G91-AR [39].

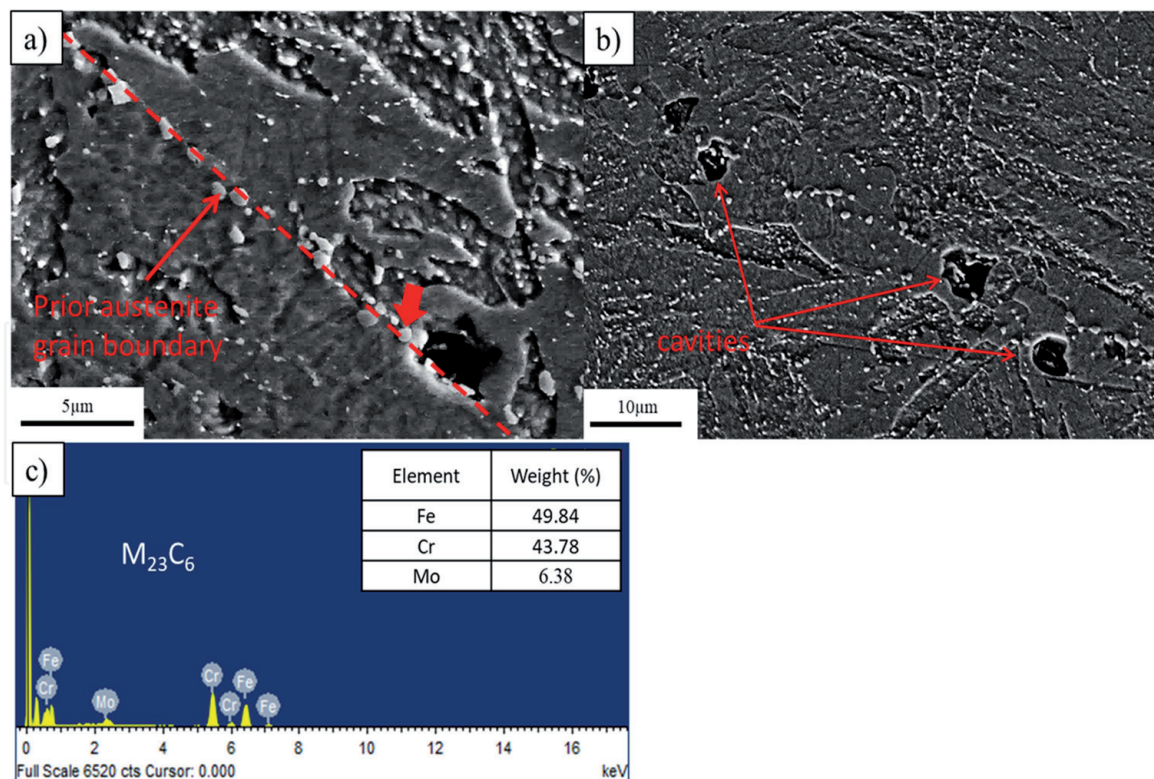


Figure 11.

Scanning electron microscopy images: (a) $M_{23}C_6$ precipitates located at a prior austenite grain boundary in sample G91-TMT 600_20. The prior austenite grain boundary in this image has been highlighted with a dash line as a guide to the eye; (b) cavities associated with coarse $M_{23}C_6$ precipitates have nucleated at a prior austenite grain boundary in sample G91-TMT 900_40. Cavities have been pinpointed with arrows and (c) EDS analysis of the particle marked with a red arrow in image (a), close to a cavity [39].

blurred in samples ausformed at 600°C because of the high deformation accumulated in the austenite during ausforming [38]. After the SPCT, it is observed that the original lath-like morphology has partially disappeared, and it has evolved towards a fine-grained equiaxed ferritic matrix. One might conclude from the microstructural observations made after SPCT that newly formed equiaxed grains are distributed homogeneously in the conventionally treated sample (AR), while these grains are located mainly nearby the prior austenite grain boundaries in the TMT samples, which is consistent with the fact that it is in these samples where the deformation accumulated is larger during creep.

Therefore, taking into account the results shown previously in the SEM micrographs (**Figure 11(a)** and **(b)**), the microstructural degradation would be a combined consequence of the accumulation of dislocations at the low-angle boundaries and the stress concentration close to the coarse $M_{23}C_6$ carbides, which lead to the progressive loss of the lath-like martensitic microstructure, which evolves to an equiaxed ferritic matrix. As it has been discussed above in the case of the TMT samples, the nucleation of cavities takes place close to $M_{23}C_6$ precipitates located at the prior austenite grain boundaries. The coalescence of the cavities formed surrounding the $M_{23}C_6$ carbides would initiate the cracks, and they will propagate along the prior austenite grain boundaries.

The more homogeneous distribution of the $M_{23}C_6$ precipitates in the conventionally treated sample favors the apparition of equiaxed grains in the whole martensitic matrix and develops the nucleation of cavities intragranularly, which provokes the transgranular fracture. Besides, in the TMT samples, the high austenitization temperature produces an enormous prior austenite grain sizes with concomitant large grain boundary surfaces, facilitating an earlier formation of the critical crack length that causes the brittle fracture [68, 69].

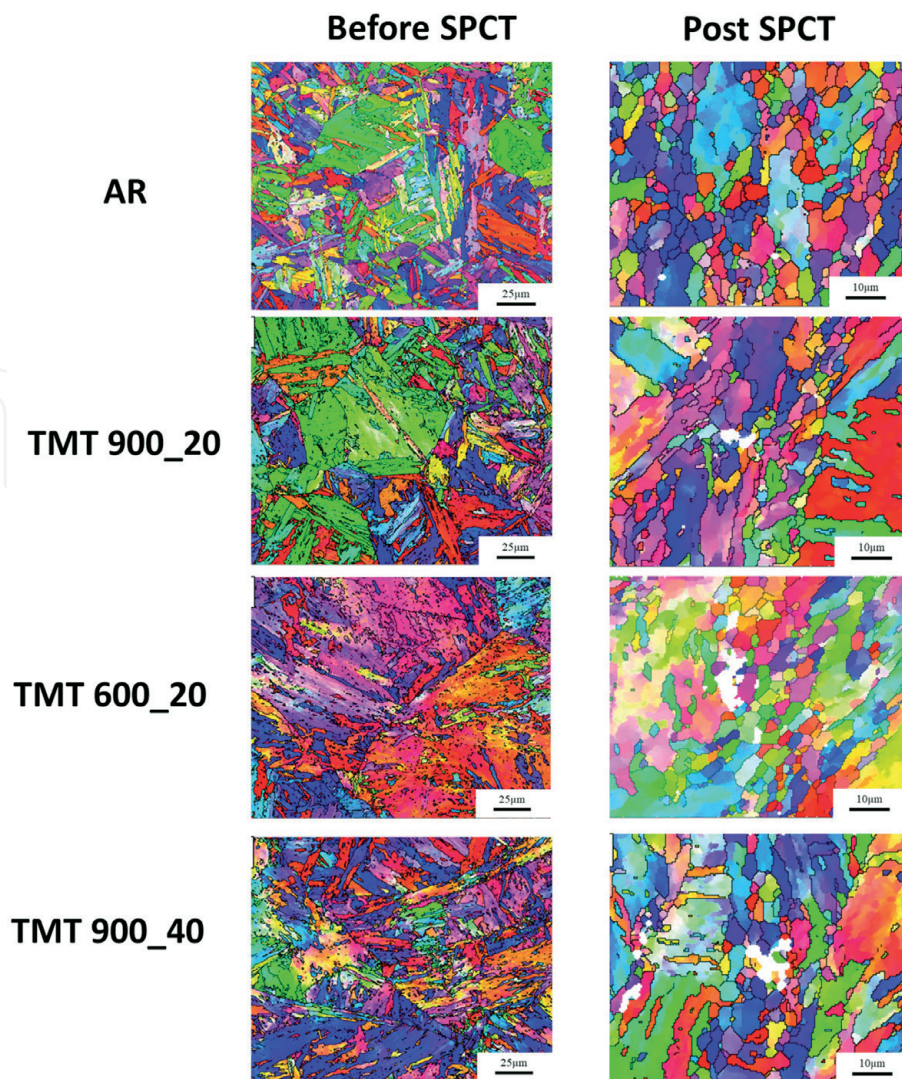


Figure 12. Representative inverse pole figure (IPF) maps of the initial and after SPCT microstructures: (a) G91-AR; (b) G91-TMT 900_20; (c) G91-TMT 600_20; and (d) G91-TMT 900_40. Cavities are in white in post-SPCT microstructures [39].

5. Conclusions

Effect of austenitization temperature: compared to the conventional heat treatments, the use of a higher austenitization temperature (1225°C rather than 1040°C), combined with an ausforming processing step at 900°C, allows the increase of the number density of MX precipitates up to three orders of magnitude after the tempering step, which raises the strengthening capability of the MX at 700°C up to 6.5 times. These microstructures have reduced considerably the minimum disk deflection rate and showed greater time to rupture during the SPCT carried out at 700°C. By contrast, such elevated austenitization temperature induces an important drop in ductility.

Effect of ausforming: the SPCT was applied to evaluate the creep behavior of G91 steel after different TMT and heat treatments. The minimum disk deflection rate was lower, and the time to rupture was longer for G91 after the TMT than with the conventional G91 heat treatment (AR). The improvement in creep rupture strength is attributed to the fine and homogeneous distribution of MX carbonitrides. The number density and average precipitate size of MX carbonitrides after the TMT are similar to the oxide particles in ODS steels. These latter steels possess high creep strength due to the high number density of oxides distributed in the

matrix. Considering the MX carbonitrides as a substitute for oxides, 9Cr FM steels after the TMT are a potential replacement of ODS steels, which are fabricated by expensive powder metallurgy and mechanical alloying processing routes.

Creep failure: based on the results presented above and taking into account the different stages of the TMT, the loss of creep ductility that enhances the change in fracture mechanism would be promoted by the coarsening of $M_{23}C_6$ carbides at the vicinity of the prior austenite grains. The coarse $M_{23}C_6$ carbides located on prior austenite grain boundaries favor the nucleation of the cavities at the vicinity of the prior austenite grains. Besides, in the TMT samples, the high austenitization temperature produces an enormous prior austenite grain sizes with concomitant large grain boundary surfaces, facilitating an earlier formation of the critical crack length that causes the brittle fracture.

Acknowledgements

We acknowledge support for the publication fee by the CSIC Open Access Publication Support Initiative through its Unit of Information Resources for Research (URICI).

Author details

Javier Vivas, David San-Martin, Francisca G. Caballero and Carlos Capdevila*
National Center for Research in Metals (CENIM), Spanish Council for Scientific Research (CSIC), Madrid, Spain

*Address all correspondence to: ccm@cenim.csic.es

IntechOpen

© 2020 The Author(s). Licensee IntechOpen. This chapter is distributed under the terms of the Creative Commons Attribution License (<http://creativecommons.org/licenses/by/3.0>), which permits unrestricted use, distribution, and reproduction in any medium, provided the original work is properly cited. 

References

- [1] Klueh RL, Gelles DS, Jitsukawa S, Kimura A, Odette GR, van der Schaaf B, et al. Ferritic/martensitic steels—Overview of recent results. *Journal of Nuclear Materials. Part 1(0)*. 2002;**307-311**:455-465
- [2] Zinkle SJ, Was GS. Materials challenges in nuclear energy. *Acta Materialia*. 2013;**61(3)**:735-758
- [3] Klueh RL, Nelson AT. Ferritic/martensitic steels for next-generation reactors. *Journal of Nuclear Materials*. 2007;**371(1-3)**:37-52
- [4] Hald J. Microstructure and long-term creep properties of 9-12% Cr steels. *International Journal of Pressure Vessels and Piping*. 2008;**85(1-2)**:30-37
- [5] Pasternak J, Dobrzański J. Properties of welded joints on superheater coils made from new generation high alloy martensitic steels connected to austenitic creep-resisting steels and super alloy grades, for supercritical parameters. *Advanced Materials Research*. 2011:466-471
- [6] Skelton RP, Gandy D. Creep-fatigue damage accumulation and interaction diagram based on metallographic interpretation of mechanisms. *Materials at High Temperatures*. 2008;**25(1)**:27-54
- [7] Klueh RL, Harries DR. High-Chromium Ferritic and Martensitic Steels for Nuclear Applications. West Conshohocken: American Society for Testing and Materials; 2001. p. 228
- [8] Abe F. Bainitic and martensitic creep-resistant steels. *Current Opinion in Solid State and Materials Science*. 2004;**8(3-4)**:305-311
- [9] Klueh RL, Ehrlich K, Abe F. Ferritic/martensitic steels: promises and problems. *Journal of Nuclear Materials. Part A(0)*. 1992;**191-194**:116-124
- [10] Masuyama F. History of power plants and Progress in heat resistant steels. *ISIJ International*. 2001;**41(6)**:612-625
- [11] Mayer KH, Masuyama F. *The Development of Creep-Resistant Steels*. Woodhead Publishing; 2008. pp. 15-77
- [12] Abe F. Coarsening behavior of lath and its effect on creep rates in tempered martensitic 9Cr–W steels. *Materials Science and Engineering A*. 2004;**387**:565-569
- [13] Fujita T. Heat-resistant steels for advanced power plants. *Advanced Materials & Processes*. 1992;**141(4)**:42-45
- [14] Vaillant JC, Vandenberghe B, Hahn B, Heuser H, Jochum C. T/P23, 24, 911 and 92: New grades for advanced coal-fired power plants-properties and experience. *International Journal of Pressure Vessels and Piping*. 2008;**85(1-2)**:38-46
- [15] Ennis PJ, Czyrska-Filemonowicz A. Recent advances in creep-resistant steels for power plant applications. *Sadhana*. 2003;**28(3-4)**:709-730
- [16] Wasilkowska A, Bartsch M, Messerschmidt U, Herzog R, Czyrska-Filemonowicz A. Creep mechanisms of ferritic oxide dispersion strengthened alloys. *Journal of Materials Processing Technology*. 2003;**133(1-2)**:218-224
- [17] Abe F. Effect of boron on creep deformation behavior and microstructure evolution in 9% Cr steel at 650°C. *International Journal of Materials Research*. 2008;**99(4)**:387-394
- [18] Eggeler G, Dlouhy A. Boron segregation and creep in ultra-fine grained tempered martensite ferritic steels. *Zeitschrift für Metallkunde*. 2005;**96(7)**:743-748

- [19] Abe F, Kern TU, Viswanathan R, editors. Creep-Resistant Steels. Materials. Cambridge: Woodhead Publishing Limited and CRC Press; 2008
- [20] Reed-hill R, Abbachian R. Physical Metallurgy Principles. Boston: PWS Kent; 1992
- [21] Norton FH. Creep of Steel at High-Temperatures. New York: Mc-Graw Hill; 1929
- [22] Langdon TG, Mohamed FA. A simple method of constructing an Ashby-type deformation mechanism map. Journal of Materials Science. 1978;**13**(6):1282-1290
- [23] Zhang XZ, Wu XJ, Liu R, Liu J, Yao MX. Deformation-mechanism-based modeling of creep behavior of modified 9Cr-1Mo steel. Materials Science and Engineering A. 2017;**689**:345-352
- [24] Abe F. Precipitate design for creep strengthening of 9% Cr tempered martensitic steel for ultra-supercritical power plants. Science and Technology of Advanced Materials. 2008;**9**(1):15
- [25] Abe F, Horiuchi T, Taneike M, Sawada K. Stabilization of martensitic microstructure in advanced 9Cr steel during creep at high temperature. Materials Science and Engineering A. 2004;**378**(1-2):299-303
- [26] Prat O, García J, Rojas D, Sanhueza JP, Camurri C. Study of nucleation, growth and coarsening of precipitates in a novel 9%Cr heat resistant steel: Experimental and modeling. Materials Chemistry and Physics. 2014;**143**(2):754-764
- [27] Abe F, Nakazawa S, Araki H, Noda T. The role of microstructural instability on creep behavior of a martensitic 9Cr-2W steel. Metallurgical Transactions A. 1992;**23**(2):469-477
- [28] Maddi L, Barbadikar D, Sahare M, Ballal AR, Peshwe DR, Paretkar RK, et al. Microstructure evolution during short term creep of 9Cr-0.5Mo-1.8W steel. Transactions of the Indian Institute of Metals. 2015;**68**(2):259-266
- [29] Ghassemi-Armaki H, Chen RP, Maruyama K, Igarashi M. Contribution of recovery mechanisms of microstructure during long-term creep of Gr.91 steels. Journal of Nuclear Materials. 2013;**433**(1-3):23-29
- [30] Klueh RL, Hashimoto N, Maziasz PJ. Development of new nano-particle-strengthened martensitic steels. Scripta Materialia. 2005;**53**(3):275-280
- [31] Hollner S, Fournier B, Le Pendu J, Cozzika T, Tournié I, Brachet JC, et al. High-temperature mechanical properties improvement on modified 9Cr-1Mo martensitic steel through thermomechanical treatments. Journal of Nuclear Materials. 2010;**405**(2):101-108
- [32] Tan L, Busby JT, Maziasz PJ, Yamamoto Y. Effect of thermomechanical treatment on 9Cr ferritic-martensitic steels. Journal of Nuclear Materials. 2013;**441**(1-3):713-717
- [33] Li S, Eliniyaz Z, Sun F, Shen Y, Zhang L, Shan A. Effect of thermomechanical treatment on microstructure and mechanical properties of P92 heat resistant steel. Materials Science and Engineering A. 2013;**559**(0):882-88
- [34] Tan L, Yang Y, Busby JT. Effects of alloying elements and thermomechanical treatment on 9Cr reduced activation ferritic-martensitic (RAFM) steels. Journal of Nuclear Materials. 2013;**442**(1-3, Supplement 1):S13-SS7
- [35] Klueh RL, Hashimoto N, Maziasz PJ. New nano-particle-strengthened ferritic/martensitic steels by conventional

thermo-mechanical treatment. *Journal of Nuclear Materials. Part A*(0). 2007;**367-370**:48-53

[36] Song M, Sun C, Fan Z, Chen Y, Zhu R, Yu KY, et al. A roadmap for tailoring the strength and ductility of ferritic/martensitic T91 steel via thermo-mechanical treatment. *Acta Materialia*. 2016;**112**:361-377

[37] Vivas J, Celada-Casero C, San Martín D, Serrano M, Urones-Garrote E, Adeva P, et al. Nano-precipitation strengthened G91 by thermo-mechanical treatment optimization. *Metallurgical and Materials Transactions A*. 2016:1-8

[38] Vivas J, Capdevila C, Jimenez J, Benito-Alfonso M, San-Martín D. Effect of ausforming temperature on the microstructure of G91 steel. *Metals*. 2017;**7**(7):236

[39] Vivas J, Capdevila C, Altstadt E, Houska M, Sabirov I, San-Martín D. Microstructural degradation and creep fracture behavior of conventionally and thermomechanically treated 9% chromium heat resistant steel. *Metals and Materials International*. 2019;**25**(2):343-352

[40] Vivas J, Capdevila C, Altstadt E, Houska M, San-Martín D. Importance of austenitization temperature and ausforming on creep strength in 9Cr ferritic/martensitic steel. *Scripta Materialia*. 2018;**153**:14-18

[41] Vivas J, Capdevila C, Altstadt E, Houska M, Serrano M, De-Castro D, et al. Effect of ausforming temperature on creep strength of G91 investigated by means of small punch creep tests. *Materials Science and Engineering A*. 2018;**728**:259-265

[42] Vivas J, Rementeria R, Serrano M, Altstadt E, San Martín D, Capdevila C. Effect of ausforming on creep strength of G91 heat-resistant steel. In:

Jeandin M, Ionescu M, Richard C, Shabadi R, Chandra T, editors. *10th International Conference on Processing and Manufacturing of Advanced Materials*, 2018. Zurich: Trans Tech Publications Ltd; 2018. pp. 400-406

[43] Capdevila C, Aranda MM, Rementeria R, Chao J, Urones-Garrote E, Aldazabal J, et al. Strengthening by intermetallic nanoprecipitation in Fe-Cr-Al-Ti alloy. *Acta Materialia*. 2016;**107**:27-37

[44] Capdevila C, Chen YL, Jones AR, Bhadeshia H. Grain boundary mobility in Fe-base oxide dispersion strengthened PM2000 alloy. *ISIJ International*. 2003;**43**(5):777-783

[45] Capdevila C, Miller MK, Chao J. Phase separation kinetics in a Fe-Cr-Al alloy. *Acta Materialia*. 2012;**60**(12):4673-4684

[46] Capdevila C, Miller U, Jelenak H, Bhadeshia H. Strain heterogeneity and the production of coarse grains in mechanically alloyed iron-based PM2000 alloy. *Materials Science & Engineering, A: Structural Materials: Properties, Microstructure and Processing*. 2001;**316**(1-2):161-165

[47] Capdevila C, Bhadeshia H. Manufacturing and microstructural evolution of mechanically alloyed oxide dispersion strengthened superalloys. *Advanced Engineering Materials*. 2001;**3**(9):647-656

[48] Capdevila C, Chao J, Jimenez JA, Miller MK. Effect of nanoscale precipitation on strengthening of ferritic ODS Fe-Cr-Al alloy. *Materials Science and Technology (United Kingdom)*. 2013;**29**(10):1179-1184

[49] Capdevila C, Miller M, Russell K. Aluminum partitioning during phase separation in Fe-20%Cr-6%Al ODS alloy. *Journal of Materials Science*. 2008;**43**(11):3889-3893

- [50] Miyamoto G, Iwata N, Takayama N, Furuhashi T. Variant selection of lath martensite and bainite transformation in low carbon steel by ausforming. *Journal of Alloys and Compounds*. 2013;**577**(SUPPL. 1):S528-SS32
- [51] Klueh RL. *Elevated-Temperature Ferritic and Martensitic Steels and their Application to Future Nuclear Reactor*. Knoxville: Oak Ridge National Laboratory; 2004
- [52] Abe F, Taneike M, Sawada K. Alloy design of creep resistant 9Cr steel using a dispersion of nano-sized carbonitrides. *International Journal of Pressure Vessels and Piping*. 2007;**84**(1-2):3-12
- [53] Abe F. Creep rates and strengthening mechanisms in tungsten-strengthened 9Cr steels. *Materials Science and Engineering A*. 2001;**319-321**:770-773
- [54] Taneike M, Abe F, Sawada K. Creep-strengthening of steel at high temperatures using nano-sized carbonitride dispersions. *Nature*. 2003;**424**(6946):294-296
- [55] Chiba T, Miyamoto G, Furuhashi T. Variant selection of lenticular martensite by ausforming. *Scripta Materialia*. 2012;**67**(4):324-327
- [56] Miyamoto G, Iwata N, Takayama N, Furuhashi T. Mapping the parent austenite orientation reconstructed from the orientation of martensite by EBSD and its application to ausformed martensite. *Acta Materialia*. 2010;**58**(19):6393-6403
- [57] Tamura I, Tsuzaki K, Maki T. Morphology of lath martensite formed from deformed austenite in 18% Ni maraging steel. *Journal de Physique (Paris), Colloque*. 1982;**321**:288-293
- [58] Brookfield DJ, Li W, Rodgers B, Mottershead JE, Hellen TK, Jarvis J, et al. Material properties from small specimens using the punch and bulge test. *The Journal of Strain Analysis for Engineering Design*. 1999;**34**(6):423-436
- [59] Kennett SC, editor. *Strengthening and Toughening Mechanisms in Low-C Microalloyed Martensitic Steel as Influenced by Austenite Conditioning*. Golden, CO, USA: Colorado School of Mines; 2014
- [60] Mitsuhara M, Yamasaki S, Miake M, Nakashima H, Nishida M, Kusumoto J, et al. Creep strengthening by lath boundaries in 9Cr ferritic heat-resistant steel. *Philosophical Magazine Letters*. 2016;**96**(2):76-83
- [61] Tan L, Snead LL, Katoh Y. Development of new generation reduced activation ferritic-martensitic steels for advanced fusion reactors. *Journal of Nuclear Materials*. 2016;**478**:42-49
- [62] Miyamoto G, Iwata N, Takayama N, Furuhashi T. Quantitative analysis of variant selection in ausformed lath martensite. *Acta Materialia*. 2012;**60**(3):1139-1148
- [63] Wakasa K, Wayman CM. The morphology and crystallography of ferrous lath martensite. *Studies of Fe-20%Ni-5%Mn—I. Optical microscopy. Acta Metallurgica*. 1981;**29**(6):973-990
- [64] Takahashi J, Kawakami K, J-i H, Kimura K. Direct observation of niobium segregation to dislocations in steel. *Acta Materialia*. 2016;**107**(Supplement C):415-422
- [65] Bhadeshia HKDH. *Bainite in Steels: Theory and Practice*. London: Maney Publishing; 2015
- [66] Toualbi L, Cayron C, Olier P, Malaplate J, Praud M, Mathon MH, et al. Assessment of a new fabrication route for Fe-9Cr-1W ODS cladding

tubes. *Journal of Nuclear Materials*.
2012;**428**(1):47-53

[67] Heintze C, Bergner F, Ulbricht A, Hernández-Mayoral M, Keiderling U, Lindau R, et al. Microstructure of oxide dispersion strengthened Eurofer and iron–chromium alloys investigated by means of small-angle neutron scattering and transmission electron microscopy. *Journal of Nuclear Materials*. 2011;**416**(1):35-39

[68] Anderson TL, editor. *Fracture Mechanics : Fundamentals and Applications*. 3rd ed. Boca Raton, FL: Taylor & Francis/CRC Press; 2005

[69] Plesiutchnig E, Beal C, Paul S, Zeiler G, Sommitsch C. Optimised microstructure for increased creep rupture strength of MarBN steels. *Materials at High Temperatures*. 2015;**32**(3):318-322

IntechOpen